Novel nuclear reactions observed in bremsstrahlung-irradiated deuterated metals

Bruce M. Steinetz [1,*] Theresa L. Benyo [1] Arnon Chait [1] Robert C. Hendricks,[1] Lawrence P. Forsley [2]
Bayarbadrakh Baramsai,[3] Philip B. Ugorowski [3] Michael D. Becks,[3] Vladimir Pines,[4] Marianna Pines,[4]
Richard E. Martin [5] Nicholas Penney [6] Gustave C. Fralick,[1] and Carl E. Sandifer, II [1]

[1]*National Aeronautics and Space Administration, Glenn Research Center, Cleveland, Ohio 44135, USA*
[2]*JWK Corporation, Annandale, Virginia 22003, USA*
[3]*Vantage Partners, LLC, Brook Park, Ohio 44142, USA*
[4]*PineSci Consulting, Avon Lake, Ohio 44012, USA*
[5]*Cleveland State University, Cleveland, Ohio 44115, USA*
[6]*Ohio Aerospace Institute, Brook Park, Ohio 44142, USA*

d-D nuclear fusion events were observed in an electron-screened, deuterated metal lattice by reacting cold deuterons with hot deuterons (d^*) produced by elastically scattered neutrons originating from bremsstrahlung photodissociation (where "d" and "D" denote ^{2}H). Exposure of deuterated materials (ErD_3 and TiD_2) to photon energies in the range of 2.5–2.9 MeV resulted in photodissociation neutrons that were below 400 keV and also the 2.45-MeV neutrons consistent with $^2\mathrm{H}(d, n)^3$He fusion. Additionally, neutron energies of approximately 4 and 5 MeV for TiD_2 and ErD_3 were measured, consistent with either boosted neutrons from kinetically heated deuterons or Oppenheimer-Phillips stripping reactions in the highly screened environment. Neutron spectroscopy was conducted using calibrated lead-shielded liquid (EJ-309) and plastic (stilbene) scintillator detectors. The data support the theoretical analysis in a companion paper, predicting fusion reactions and subsequent reactions in the highly screened environment.

I. INTRODUCTION

In the pursuit of understanding astrophysical processes and effects of electron screening in fusion processes, many in the field [1–7] have performed studies by directing deuteron beams into deuterated metal substrates and have measured substantially increased reaction rates over gas targets. The electron clouds in the metal targets act to screen the positive ion charge, whereby the projectile deuteron (d) effectively sees a reduced electrostatic barrier, leading to higher cross sections for d-D fusion than for bare nuclei. (Here and throughout the text "D" denotes ^{2}H.) The community introduced the concept of screening potential U_e to increase the probability of quantum tunneling by a uniform negative shift $-U_e$ of the Coulomb barrier $U_c(r)$ [8]. Researchers have found U_e ranging from $\approx$25 eV for gaseous targets [9], to $\approx$50 eV for deuterated insulators and semiconductor targets [5,6,10,11], and to much higher levels for metals such as beryllium (180 eV) and palladium (800 eV) [5,6,11].

In a companion theoretical paper by Pines *et al.* [12], we introduce a theoretical approach to combine the previously recognized lattice and shell electron contributions to screening, along with screening by plasma created from ionization channels temporally generated from γ irradiation, into an enhanced screening energy U_e and utilize the concept of an enhancement factor $f(E)$ to relate bare cross sections to those experimentally observed [8]. The experimental fusion cross section $\sigma_{\exp}(E)$ can be written as

$$\sigma_{\exp}(E) = \sigma_{\mathrm{bare}}(E) \times f(E). \quad (1)$$

Here, the enhancement factor is formulated as

$$f(E) = \frac{S(E + U_e)}{S(E)} \frac{E}{(E + U_e)} \exp\{G(E) - G(E + U_e)\}, \quad (2)$$

where $G(E)$ is the Gamow factor; $S(E)$ is the astrophysical S-factor, and E is the projectile energy.

In Ref. [12] we show that screening is effective not only to enhance nuclear tunneling but also to increase the probability of Coulomb scattering at large angles. Without screening, low-angle scattering of hot charged "projectiles" dominates, resulting in nonproductive elastic scattering and reduced tunneling. Therefore, efficient electron screening is a necessary ingredient for inducing and sustaining nuclear fusion.

From the analysis in Ref. [12] it is also evident that an optimal way to exchange kinetic energy between particles would involve uncharged particles. Neutrons have high scattering cross sections on nuclear fuel (e.g., deuterons), and can deliver a substantial portion of their kinetic energy in a single elastic collision to the deuteron.

Here, we demonstrate the impact of efficient electron screening on localized fusion rates in a dense-fuel environment. Such an environment features the fuel at a very high-number-density state, together with efficient screening

*Corresponding author: bruce.m.steinetz@nasa.gov

by shell, conduction, or plasma electrons. Based on analysis results in Ref. [12], we exploit neutrons to effectively heat deuterons. Hot neutrons originate from photodisintegration of deuterons bombarded by photons above the 2.226 MeV level. The hot neutrons scatter and efficiently deliver nearly one-half of their energy to a deuteron (n, d). The hot deuteron is then able to be scattered at a large angle with a nearby cold deuteron in a highly screened environment, leading to efficient nuclear tunneling and fusion $(D + d \rightarrow n + {}^3\text{He})$. Maintaining one of the two fusing nuclei as a cold ion screened by electrons provides for highly efficient large-angle scattering and subsequent tunneling probabilities. This fusion cycle is performed at high fuel density inside a metal lattice to enable subsequent reactions with the host metal nuclei and other secondary processes. It is noted that the efficient scattering process described in this strongly screened environment is fundamentally different than other fusion processes (e.g., magnetic confinement, tokamak) in which all of the fuel nuclei are hot and reside in a weakly screened environment. Such an environment is dominated by small-angle, nonproductive elastic Coulomb scattering with less efficient tunneling probability.

We examined herein a fusion process in which kinetic energy exchange from hot neutrons to the fuel provides the basis for fusion initiation and potential secondary nuclear events. Secondary processes following the initial fusion event include kinetically heated (d^*) boosted fusion reactions $(D + d^* \rightarrow n^* + {}^3\text{He})$, conventional secondary channels with ${}^3\text{He}$, t, α particles, etc., and potentially highly energetic interactions with the metal lattice nuclei, including Oppenheimer-Phillips stripping processes [13].

The goal in this study was to explore fusion processes that make optimal use of strongly electron-screened environments, with high-density fuel, in a manner conducive for process multiplication via effective secondary reactions. The experimental campaign described here was guided by the companion theoretical work by Pines *et al.* [12] and the novel reactions observed in Steinetz *et al.* [14], Benyo *et al.* [15], Belyaev *et al.* [16], and Didyk and Wisniewski [17] using bremsstrahlung radiation.

II. EXPERIMENTAL SETUP, DATA ACQUISITION, AND ANALYSIS

A. Electron accelerator and general layout

Tests were performed using a Dynamitron electron accelerator having independent control of beam energy (450 keV to 3.0 MeV) and beam current (10–30 mA), as shown in Fig. 1(a). The direct-current electron beam enters the beam room via an evacuated tube and is scanned over the braking target, utilizing the scanning magnet ≈ 1 m above the target. The beam was operated in photon mode for the current tests, utilizing a 1.2-mm-thick tantalum braking target. Samples in glass vials were placed on an aluminum exposure tray close to the tantalum braking target and were exposed while the electron beam scanned at a frequency of 100 Hz over the length of 0.91 m. Figures 1(a) and 1(b) show the relative positions of the 16 samples (total length 0.46 m) and
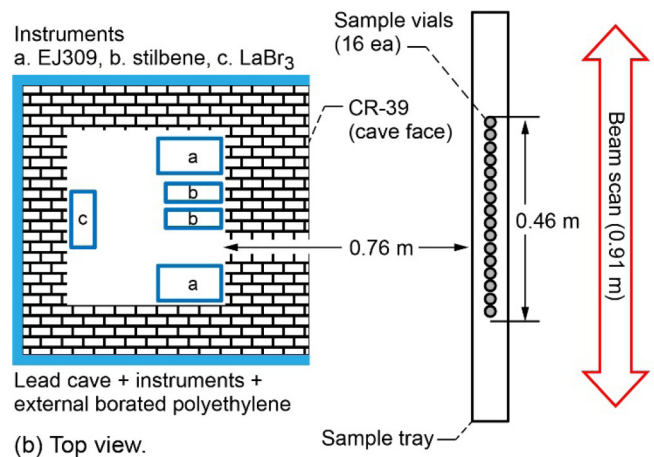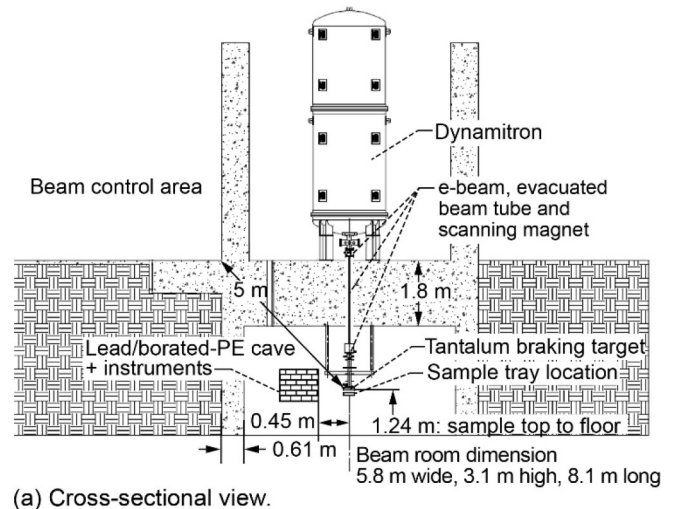

(a) Cross-sectional view.

(b) Top view.

FIG. 1. Schematic of beam, samples, cave, and instruments. (a) Overall cross-sectional view of setup; (b) top view of test samples, cave (top removed), instruments, and beam scan.

the lead cave, which housed the neutron detectors and will be described below. Figure 2(a) illustrates the close proximity (11.2 mm distance) of the 20-ml sample vials relative to the braking target, which was cooled with ambient-temperature water flowing spanwise in a stainless-steel cooling channel. Figure 2(b) illustrates how the beam scanned back and forth over the 16 glass vials.

B. Cave description

Because of the intense γ flux, the detectors were placed in a lead cave with the following wall thicknesses: front wall, 30.5 cm (12 in.); top and side walls, 15.3 cm (6 in.); and base and rear walls, 10.1 cm (4 in.). The distance from the sample centerline to the faces of the scintillator detectors was 0.76 m (30 in.) [Fig. 1(b)]. Borated polyethylene (B-PE) was used to reduce the large flux of thermal neutrons entering from the sides of the cave to minimize the γ signals from the reaction $\text{Pb}(n, \gamma)$ from the cave walls, thereby improving signal quality. The B-PE thickness was 2.5 cm for the top,
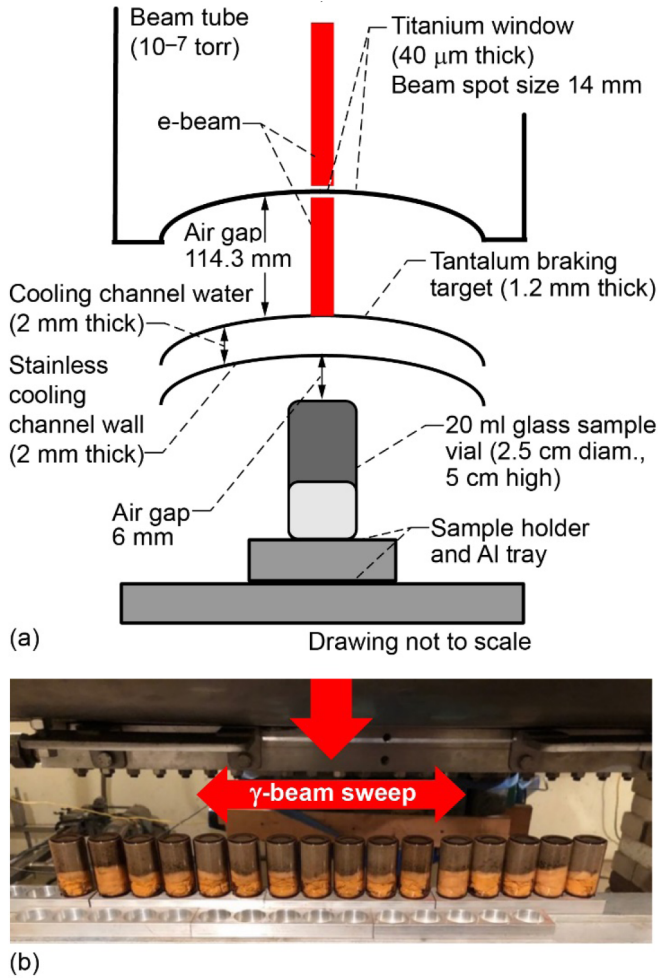
(a)

(b)

FIG. 2. (a) Cross section of electron beam, titanium vacuum window, tantalum braking target, stainless-steel cooling channel, and sample; (b) photograph of specimens in glass vials.

sides, and back of the cave, and 2.5-cm B-PE plus 5-cm normal high-density standard PE were used for the cave base.

C. Beam characteristics

1. Photon flux

The high-flux Dynamitron electron beam struck a tantalum target, exposing the samples to intense bremsstrahlung radiation. Figure 3 provides the photon spectrum $N_\gamma (E_\gamma)$ for the peak electron beam energy end point of 2.9 MeV at the top of the sample, as determined using the fitted five-term interpolation formula, following Refs. [18,19] for 450 μA of current (per vial):

$$N_\gamma(E_\gamma) = (c_0 + c_1 \cdot E_\gamma)\left(\frac{E_\gamma}{E_\gamma^{\mathrm{max}}}\right)^{\alpha_0 + \alpha_1 \cdot E_\gamma}\left(1 - \frac{E_\gamma}{E_\gamma^{\mathrm{max}}}\right)^{\beta},$$

(3)

where E_γ^{max} is maximum photon energy per one incident electron and E_γ is photon energy in MeV, with $N_\gamma (E_\gamma)$ in units of photon/(second megaelectronvolt steradian). Constants used
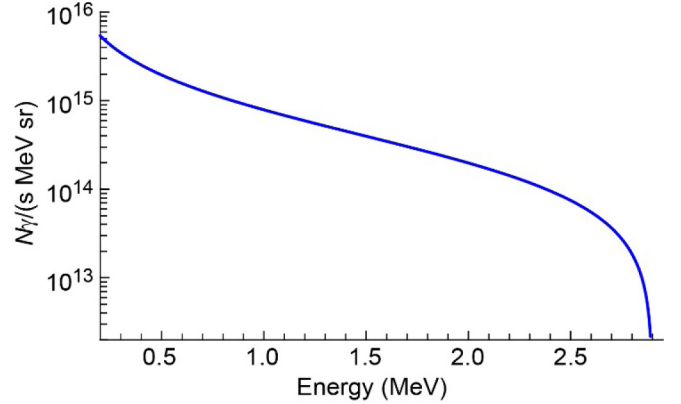

FIG. 3. Bremsstrahlung photon spectrum for electron beam endpoint of 2.9 MeV, for 450-μA (per vial) test case (top of sample).

were $c_0 = -3.187 \times 10^{-3}$ Photons/(sec-MeV-steradian), $c_1 = 3.506 \times 10^{-3}$ Photons/(sec-MeV^2-steradian), $\alpha_0 = -2.035$, $\alpha_1 = -3.189 \times 10^{-2}$ 1/MeV, and $\beta = 6.327 \times 10^{-1}$. The peak photon energy was corroborated by the lanthanum bromide (LaBr$_3$) γ detector mounted in the cave. The photon flux plotted in Fig. 3 was corroborated by a Monte Carlo (MCNP® [20]) analysis modeling the geometry noted in Fig. 2.

2. Photodissociation neutrons

With the beam operating above the deuteron photodissociation energy (2.226 MeV), photoneutrons were produced. The peak and nominal photodissociation neutron energies were calculated via Ref. [21], as shown in Table I.

D. Neutron detection

1. Prompt neutron detection

Three different neutron detection systems were employed as noted in Table II. The EJ-309 liquid scintillator (Eljen Technology) and the stilbene single-crystal detector (Inrad Optics) were used to detect prompt fast-neutron counts and energies. The Eljen detector (5 cm diam. by 10 cm long), being larger than the stilbene detector (2.5 cm diam. by 2.5 cm long), had a higher sensitivity to the fast neutrons, resulting in greater signal strength. Yet because of the unique single-crystal material, the stilbene could measure slightly lower energy (0.3 MeV threshold) neutrons as opposed to the EJ-309 (0.5 MeV threshold). Both detectors pointed toward the

TABLE I. Calculated photodissociation neutron energies.

Beam energy (MeV)	Neutron energy (MeV)		
	Nominal energy	Aligned with beam (0° direction)	Counter to beam (180° direction)
2.5	0.135	0.144	0.127
2.7	0.235	0.246	0.224
2.9	0.335	0.348	0.321
3.0	0.385	0.399	0.370

TABLE II. Neutron detection instrument details.

Detector	Detection technology (manufacturer)	Detector material	Detector dimensions (cm)	Location (distance from specimens) (as noted)	PMT voltage (V)	Energy detection (MeV)
Eljen-309 (HV)	Liquid Scintillator; proton recoil (Eljen)	Xylene-based liquid	5 cm diam. by 10 cm long	In cave (0.76 m)	−1,100	Neutron: 0.5–15
stilbene (St1)	Plastic, single crystal; proton recoil (Inrad Optics)	Stilbene crystals wrapped in PTFE tape; optically polished on face + fused silica window	2.5 cm diam. by 2.5 cm long	In cave (0.76 m)	730	Neutron: 0.3–15
LaBr$_3$	LaBr$_3$ detector (Canberra)	LaBr$_3$ crystal	3.8 cm diam. by 3.8 cm long	In rear of cave, rotated 90° and offset toward entry door	730	0–10[a]

[a]Detector efficiency; γ: $\approx$ 15% for <1 MeV; $\approx$5% for 1–4.4 MeV; and 0.1% for > 4.4 MeV (characterization of PARIS LaBr$_3$(Ce)-NaI(Tl) phoswich detectors up to E_γ about 22 MeV, C. Ghosh *et al.*)

specimens during radiation and were shielded from the intense γ rays by the 30.5-cm-thick front lead wall and surrounding cave. It was found that the stilbene detector exhibited greater discrimination between photons and neutrons because of its material and design. A LaBr$_3$ γ detector was also placed in the cave (near the rear) and was used to measure γ energies from both the beam and from thermal neutron capture [Pb(n, γ)] on the lead walls. A rough estimate of photoneutrons interacting with the cave was determined by counting the 3- to 8-MeV γ's created during beam-on conditions. It is previously noted that to reduce the γ glow within the cave to acceptable levels, B-PE was placed on all five sides of the cave except the front, thereby minimizing the captured thermal neutrons to reduce the ionizing radiation from the Pb(n, γ). By using the B-PE around the cave, higher beam currents could be used, thereby increasing process signal-to-background noise for the fueled shots, to meet the goal of accurately measuring fusion and other reaction neutrons.

2. Prompt neutron signal postprocessing

High-intensity primary bremsstrahlung and secondary fluorescence x-rays from the Dynamitron beam were the major challenges for postprocessing the detector signal, even though the detectors were shielded in the lead cave. The strategy was to record all detector signals without any information loss with the fast data acquisition system throughout the beam exposure. We developed a sophisticated model-based pulse shape discrimination (PSD) signal analysis procedure for the postprocessing data analysis, which is further described in Sec. II D 4.

The detector photomultiplier tube (PMT) signal output was directly connected to the CAEN 8-channel DT5730 desktop digitizer with 500-MHz sampling rate and 14-bit resolution, which is well suited for the organic scintillator signal. The digitizer's pulse-processing- (DPP-)PSD firmware and control software, CoMPASS, is used for the on-line signal processing, data acquisition monitoring, and waveform recording. Each detector signal is triggered locally at the input channel and recorded independently with the DPP firmware. The digitizer's USB 2.0 interface allows data transfer up to 30 MB/s. During the experiment the data transfer speed was monitored, and data overflow was prevented by increasing the detection threshold, reducing the beam current, reducing the number of detector channels, or increasing the shielding materials. A total of 140 samples (280 ns long) of each signal waveform was recorded for the postprocessing.

3. Energy calibration

The energy scales of the detector's pulse height spectrum were periodically calibrated using ^{137}Cs, ^{60}Co, and ^{232}Th check sources. The PMT gains and calibration stability were important for the PSD performance, the neutron spectrum unfolding, and combining and/or comparing separate sets of experimental data. The detector gain stability across the measurements was confirmed (and corrected) using the 511 keV line during off-line instrument checks. The detector's neutron detection efficiency was determined from the well-known spectra of the AmBe and ^{252}Cf sources. Average

detector efficiency was calculated to be approximately 13% for the stilbene detectors and 11% for the EJ-309 detectors. Energy-dependent efficiency was used for the response matrix normalization and subsequently for the neutron flux calculation of the detector unfolding.

4. Signal filtering and hybrid PSD approach

A two-stage process was used to process the scintillator data. First, the signal was filtered with a multistep approach to arrive at a series of clean waveforms. Second, the hybrid PSD analysis was used to virtually eliminate false neutron counting, which extends the work of Refs. [22,23]. The most important filter to remove double peaks and false neutron counting is the pile-up signal rejection (PUR) filter [24]. If small peaks (spikes) with amplitudes exceeding 8% of the main peak were observed on the tail of the signal, it was rejected from further processing. The rejection criterion was set to 5% for the stronger signals above 1 MeV. The PUR criteria cannot be tighter because it is the delayed secondary scintillator phosphorescence light pulses that give the PSD information. Next, low-amplitude high-frequency noise filters incorporating a root-mean-square (RMS) approach were applied to remove the smaller x-ray signals (spikes) and delayed fluorescence, which might pass through the pile-up rejection criteria. Also, successive neutron recoils within the phosphorescence decay will alter PSD performance. These types of events were further reduced by the signal RMS and baseline shift filters. The pile-up rate increases with the beam energy and current. Additional details regarding factors influencing detector efficiency are presented in Sec. IV A 2.

The clean wave forms were subsequently processed by the hybrid PSD algorithm. The PSD processing also consisted of a multistep approach. The signal was first processed through a frequency-gradient method with fast-Fourier transform (FFT) and wavelet analysis [25,26]. Next, each signal was compared to a predetermined neutron or γ template waveform [22]. Finally, the charge integration method [27] was then applied, comparing the tail area to the overall area, resulting in plots of PSD parameter versus electron equivalent energy, as will be shown in Sec. III. Because of the high γ flux, the waveform was accepted as a neutron if the PSD parameter was above an 8σ threshold of the γ-ray band. Therefore, accepted waveform shapes reliably resulted in neutron signatures. The PUR algorithm coupled with the 8σ constraint between the neutron and γ PSD parameter virtually eliminated neutron double hits (aliasing) and γ signals being recorded as neutrons. The 8σ constraint reduced fast-neutron counts considerably, but significantly increased the fidelity of the overall data and the neutron energy measurement. For reference purposes, the peak photoneutrons produced were less than 400 keV. This was below the Eljen-309 threshold and was also below the stilbene ability to measure because of the 8σ constraint window used to ensure separation of neutrons from γ's in the PSD.

5. Neutron energy determination

As mentioned earlier, the detectors were calibrated in electron-equivalent units, as were the measured neutron pulse height spectra. The steps used to unfold the detector response and determine the actual neutron energy spectra include the following. First, MCNPX®-PoliMi[1] and MPPost postprocessing codes were used to generate the detector response matrix. The response matrix is the ideal pulse height spectra for monoenergetic neutrons hitting the detector. The simulations utilized 1×10^8 particles (neutrons) in each of 50 keV bins over the energy range of 100 keV to 15 MeV. Next, the HEPROW computer code package [28] obtained from Oak Ridge National Lab (Radiation Safety Information Computational Center, RSICC), which used Bayes's theorem and maximum entropy methods, was utilized for the spectrum unfolding. Subsequently, three different unfolding codes were evaluated: GRAVELW, UNFANAW, and MIEKEW. A calibration study was performed in which a 40-mCurie AmBe neutron source was placed near the scintillator detectors while data were collected. Good correlation was found across the energy range when comparing the AmBe unfolded results with the well-known AmBe spectrum. The best correlation was found using the GRAVELW unfolding code, which was subsequently used for the final results reported. The input files of the unfolding code are the experimental spectra and the detector response matrix. Neutron count uncertainty is assumed to be the standard uncertainty assigned to contents in one channel, assuming Poisson statistics hold, and is the square root of the number of counts. It is also assumed that no correlation exists between different channels. The neutron penetration through the cave (lead and B-PE) was simulated using the MCNP6®[2] code [29]. For reference purposes, the lead cave scattered approximately 80% of incoming fusion neutrons.

E. Sample materials and methodology

1. Sample materials

The samples exposed in this study were created from prepared batches of either deuterated or bare (no-load) erbium or titanium metals. Table III provides the materials, test shot identifier, shot durations, energy, and current settings used. Note test shots TS1575 and 1576 were distinct samples made from ErD_3 and were exposed to evaluate reproducibility. These samples evaluated reproducibility of the process using specimens made from different material batches and exposed on different test days, and the outcomes are comparable. Samples were tracked using meticulous records for custody control from material loading through exposure and posttest analysis using high-purity germanium (HPGe) γ scans and liquid β scintillator counting.

For each test, the samples were placed into glass vials and subsequently positioned at a close distance to the tantalum braking target [Fig. 2(a)] to maximize the flux per unit area per unit time in order to evaluate the hypothesis that fusion events could be initiated with ionizing radiation in deuterated metal lattices where the deuterium fuel was in a stationary center-of-mass frame. Natural-abundance erbium (99% purity) and

―――――

TABLE III. Test shot sample exposure: ErD_3 (480 g in 16 vials) and TiD_2 (216 g in plate and powder form), showing beam parameters and durations. Note for ErD_3 and TiD_2 exposures: 5×10^{24} D atoms in samples; Bare: No D atoms added to samples.

Test shot ID	Material	Exposure duration (min)	Beam Energy (MeV)	Current (mA)
TS 589 (a,a2,f,g, Rd)	Er, bare	270	2.9	15
TS 589Ra	Er, bare	30	2.5	15
TS 589b2	Er, bare	30	2.7	15
TS 589c2	Er, bare	30	2.8	15
TS 589d2	Er, bare	30	3.0	15
TS 589Rb	Er, bare	30	2.9	5
TS 589Rc	Er, bare	30	2.9	10
TS 589Re	Er, bare	15	2.9	25
TS 589Rf	Er, bare	15	2.9	30
TS1575 (a,Ra,Rb)	ErD_3	360	2.9	15
TS1575Rb	ErD_3	30	2.9	5
TS1575Rc	ErD_3	30	2.9	10
TS1575Rd	ErD_3	30	2.9	20
TS1575Re	ErD_3	15	2.9	25
TS1575Rf	ErD_3	15	2.9	30
TS1576 (c,c2,e,Rb)	ErD_3	360	2.9	15
TS1576Ra	ErD_3	60	2.5	15
TS1576a	ErD_3	30	2.7	15
TS1576b	ErD_3	30	2.8	15
TS1576d	ErD_3	30	3.0	15
TS(610,611, 611R,612)	TiD_2	330	2.9	15
TS631	Ti, bare	60	2.9	15

Legend
Baseline configuration
Beam energy study
Beam current study

titanium (99% purity), were deuterated by gas loading using appropriate pressure, temperature, and time protocols. Erbium was chosen for this study for several reasons: (i) Erbium loads to ErD_3 having a high fuel number density (8×10^{22} D atoms/cm^3); (ii) Erbium showed enhanced nuclear reactions via LINAC exposure in previous tests [14]; (iii) Erbium metal maintains a high deuteron stoichiometry between furnace D loading and testing; and (iv) Erbium with $Z = 68$ provided a good test case for assessing the effect metal lattice screening has on reaction rates (see Ref. [12]). Titanium was also exposed under comparable conditions to examine the effect of a higher fuel number density (1×10^{23} D atoms/cm^3) and lower atomic mass ($Z = 22$), approximately one-third the positive nuclear charge of erbium, which also contributed to fewer metal lattice screening electrons. The sample mass change (accuracy $\pm 5\%$) from before until after gas loading was used to determine the D loading of the sample materials. Note 99.999% ultra-high-purity gas was used to deuterate the samples. Although the vials were sealed during exposure, ambient air was used as the cover gas.

2. Case-control methodology

A case-control methodology was utilized, where identical tests were performed on fueled (or deuterated metal) and unfueled samples (bare or nondeuterated metal), to isolate the fuel as the only experimental variable. For consistency between the fueled ErD_3 and TiD_2, the same amount of fuel (5×10^{24} D atoms) was exposed. This amounted to 480 g of ErD_3 or 216 g of TiD_2, exposed in 16 vials. For the unfueled case, comparable masses of bare erbium and bare titanium were exposed. As will be shown in Sec. III during unfueled shots there was some neutron activity above cosmogenic background. This activity is believed to have been caused by screened reactions from the naturally occurring deuterium (153 ppm) in various water-cooling passages in the Dynamitron that were exposed to either direct or indirect γ irradiation. For reference: the braking target cooling channel contained 1.6×10^{22} D atoms, and the scanner-side cooling passages contained 1.2×10^{22} D atoms.

III. EXPERIMENTAL RESULTS

A. Pulse shape discrimination spectra

Figure 4(a) provides an example of the PSD plots showing the PSD parameter versus electron equivalent energy (keVee) recorded in the detector (EJ-309 HV) for TS1576 ErD_3 with beam conditions of 2.9 MeV and 15 mA and a 6-h exposure. As previously noted in Sec. II D an 8σ constraint window was used to ensure separation of neutrons from γ's. Data points occurring above the 8σ separator line were confidently counted as neutrons and not γ's. Figure 4(a) illustrates bracketed nominal energy ranges (ranges 1 and 2) corresponding to those counts from the PSD plot, which when unfolded lead to the nominal 2.45 and 4 MeV neutron energies (see next sections for additional details).

B. Comparison of fueled and unfueled results

As described before, a case-control methodology was followed, where fueled (ErD_3, TiD_2) samples and unfueled (Er-bare, Ti-bare) samples were exposed in separate exposures, holding constant all other experimental parameters including sample material type and mass, beam energy and current, sample placement under the beam, detector placement, and cave configuration. Figure 4(b) presents the EJ-309 detector results for TS1576 (fueled) and TS589 (unfueled) in detector counts (PMT counts after filtering using the process noted earlier) versus electron energy equivalent units (keVee). Figure 4(c) presents a comparison of the net counts [TS1576 (fueled) minus TS589 (unfueled)] prior to unfolding with the HEBROW algorithms and shows the results of two relevant simulation cases. The 6-h data show significantly higher detector counts during the fueled exposures. In the simulations, a monochromatic neutron source with neutron energies (E_n) of either 2.45 or 4 MeV are used as the input to the MCNPX-Polimi model of the EJ-309 detector. The fusion energy neutrons result in simulated detector spectra centered on the main peak. The detector counts for 4-MeV neutrons have a broader energy response and correlate with the higher-energy measured counts. It is noted that the shape of the curve for
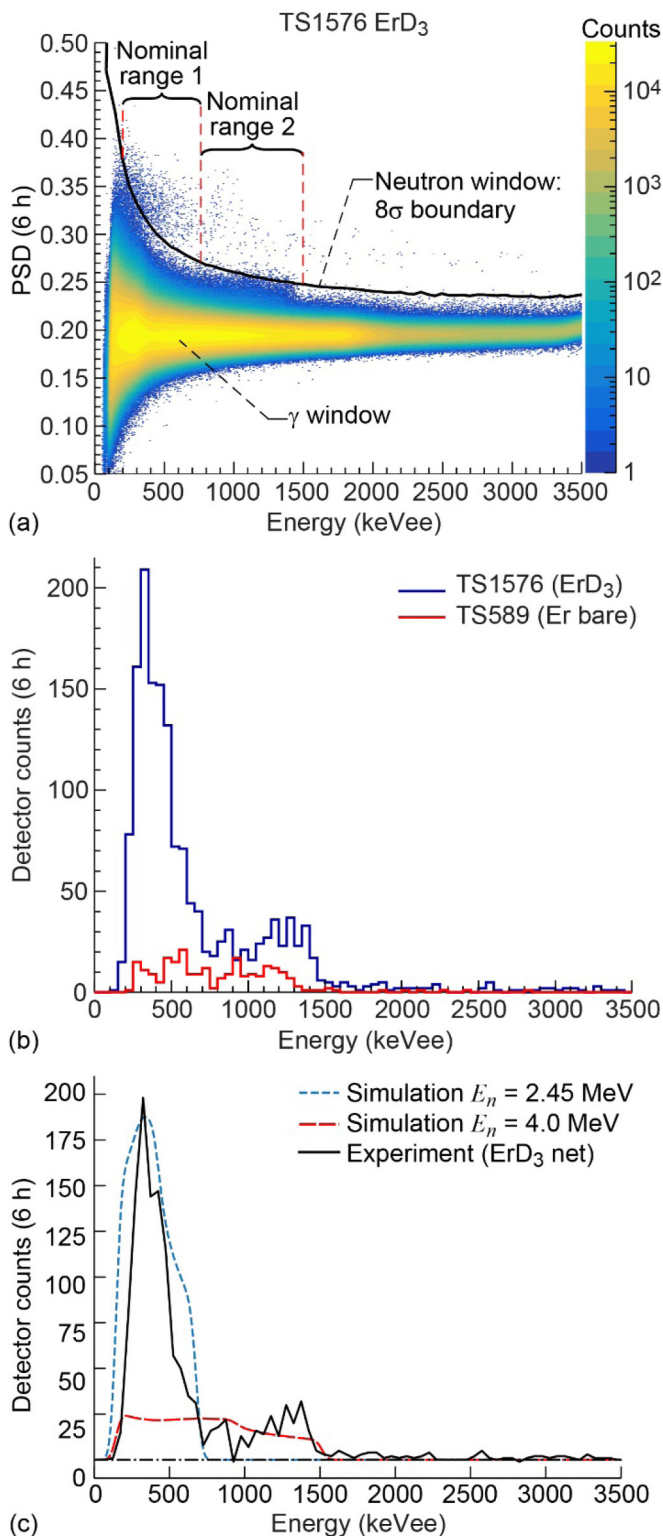
FIG. 4. Measured test data (EJ-309 HV detector) prior to unfolding (Beam 2.9 MeV, 15 mA, 6 h). (a) PSD plot for TS1576 utilizing the 8σ constraint window used to ensure separation of neutrons from γ's. (b) Detector-measured counts for TS1576 (blue, ErD_3) and TS589 (red, Er-bare) versus energy (50-keVee bins); (c) Comparison of measured net counts for ErD_3 (black, solid) with two detector simulations for a source of monochromatic neutrons with energies (E_n) of 2.45 MeV (blue, dashed) and 4 MeV (red, dashed). For

ErD_3 in the 0–800 keVee range bears significant resemblance to that in Ref. [30], where a similar scintillator/PSD approach was used to measure neutron energies for a 35-DD-W-S NSD/Gradel-Fusion d-D fusion neutron generator.

C. Neutron spectra and process reproducibility

Utilizing the methods for the detector modeling and neutron energy unfolding mentioned earlier, the net (fueled minus unfueled) PSD data were converted into neutron spectra. Figure 5 presents data showing neutron spectra measured for the 6-h aggregate data for two separate ErD_3 test samples, Fig. 5(a) for TS1575 and Fig. 5(b) for TS1576, both corrected for background and unfueled exposure. The HEBROW unfolding algorithm incorporates the instrinsic detector efficiency. The unfolded neutron spectra show a number of interesting features, including several primary neutron energy peaks of 2.45, 4, and (to a lesser degree) 5 MeV, and an apparent shoulder peak at 4.2 MeV. The measured neutron energies were remarkably close, indicating process reproducibility. Figure 5(c) shows the neutron spectra for TS1575 measured using the solid-state stilbene detector, showing the nominal 2.45-MeV fusion neutron peak, which was in the calibrated range of the detector. The higher-energy peaks occur in the nonlinear range of the detector and are not presented here.

D. Alternate material exposure: Titanium deuteride

Figure 6 shows the neutron spectra for TiD_2 using the EJ-309 detector for the net fueled (TS610 to 612) minus unfueled (TS631) PSD data. The unfolded neutron spectra show a number of interesting features, including several primary neutron energy peaks of 2.45 MeV (fusion energy), 4 MeV, and (to a lesser degree) 5 MeV, and an apparent shoulder peak 4.2 MeV. It is noted that the fluence of the fusion-energy neutron peak (≈ 2.45 MeV) is approximately 30% higher for the TiD_2 than for the ErD_3, accounting for the exposure times.

E. Comparison of TiD_2 and ErD_3 neutron production

Fusion energy neutrons. Comparing integrated fusion neutron counts of TiD_2 and ErD_3, one finds TiD_2 produces 1.31 times more neutrons than ErD_3. Recall that fusion reaction rates are proportional to the D-fuel number density squared (n^2). TiD_2 has slightly higher number density (1×10^{23} D/cm^3) than ErD_3 (0.8×10^{23} D/cm^3). Squaring the ratios of the number densities one would expect to measure approximately 1.56 greater fusion neutrons for TiD_2 than for ErD_3. It is recognized that if the number density of TiD_2 were just slightly less (0.92×10^{23} vs. 1×10^{23} D/cm^3), one could account for the small discrepancy.

Higher-energy neutrons (≈ 4 MeV). Higher counts of ≈ 4-MeV neutrons were measured for ErD_3 than for the TiD_2. This general trend would be in alignment of screened

reference purposes, the simulation results were scaled as follows: 2.45 MeV spectrum per neutron was scaled up by 17000 and the 4 MeV neuton spectrum was scaled up by 6000 to roughly match the area under the experimental curves. (For color figure see online version.)
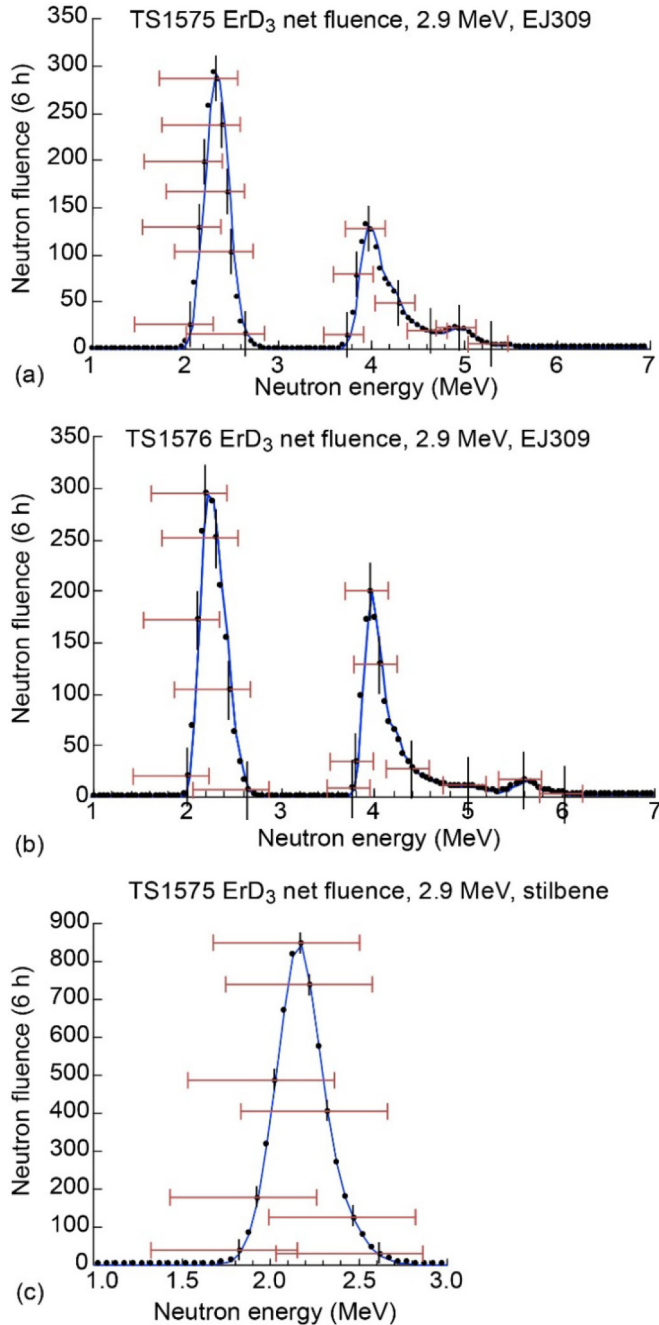
FIG. 5. Neutron spectra for ErD_3 (a) TS1575 (6 h EJ-309), (b) TS1576 (6 h EJ-309), and (c) TS1575 (6 h stilbene) net neutron counts (beam: 2.9 MeV, 15 mA), showing evidence of (1) fusion neutron production, (2) neutrons with greater than fusion energies (EJ-309), and (3) reproducibility of process. Notes: (i) Uncertainty bars represent 3σ. (ii) Fusion energy neutron counts scaled to sample location. TS1575: $1.5 \pm 0.3 \times 10^3$ neutron counts per second and TS1576 $1.6 \pm 0.3 \times 10^3$ neutron counts per second using EJ-309 and $1.4 \pm 0.2 \times 10^4$ neutron counts per second using stilbene detector. (Note: stilbene exhibits better γ-neutron separation; thus, fewer true neutrons are discarded during postprocessing, resulting in the higher neutron count rate.)
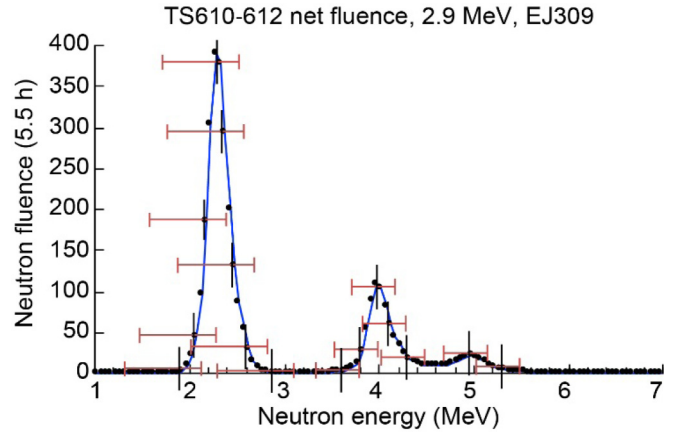

FIG. 6. Neutron spectra for TiD_2 (TS610 to 612) (5.5-h EJ-309) net neutron counts (Beam: 2.9 MeV, 15 mA), showing evidence of (1) fusion neutron production and (2) neutrons with greater than fusion energies. Notes: (i) Uncertainty bars represent 3σ. (ii) Fusion energy neutron counts scaled to sample location 1.8×10^3 neutron counts per second using EJ-309.

Oppenheimer-Phillips reactions favoring higher Z base metals. However, because there are other factors at work (i.e., neutron energy boosting) occurring simultaneously, additional research is needed to understand the differences in the 4-MeV neutrons production found for TiD_2 and ErD_3.

F. Measurement uncertainty

The uncertainty bars for the neutron spectra in Figs. 5, 6, and 7(a) were determined based on the combined effect of detector energy resolution and the unfolding algorithm. The neutron energy uncertainty (horizontal band) was determined using the perturbation method. First, the standard deviation in electron equivalent units was determined by examining the response of the detectors to established γ peaks for standard check sources (^{137}Cs and ^{60}Co) by fitting a Gaussian distribution, resulting in a σ of ≈ 50 keVee. To obtain the plotted 3σ the original spectrum was offset by either $+150$ or -150 keVee, corresponding to $\pm 3\sigma$ on the EJ-309 detector energy resolution (or ± 120 keVee for the slightly better resolution stilbene detector) prior to unfolding. Then once unfolded, the shifts in the neutron energy peaks (e.g., fusion neutron peak at 2.4 MeV) were determined for both the plus and minus unfolded spectra. This perturbation analysis resulted in a slightly asymmetric neutron energy uncertainty band, biased toward the lower energy, as shown in the figures. The fluence uncertainty (vertical bands) were determined using the GRAVELW unfolding methodology using $\pm 3\sigma$ [28]. Note: for clarity the uncertainty bars were plotted on the figures for only select data points.

IV. DISCUSSION

A. Evidence of fusion and fast neutrons

1. Fusion neutrons

As noted in Fig. 5, there are several distinct peaks corresponding to primary fusion neutrons as well as neutrons

TABLE IV. Calculated neutron energies resulting from kinetic heating of ^{2}H(D) fuel.

Generation	Reaction	Cross section (b)	Projectile neutron energy, E_n (MeV)	Product deuteron energy range, E_{d^*} for n-recoil angle: 0° to 180° (MeV)	Total energy[a] ($Q + E_{d^*}$) (MeV)	Product neutron energy range, E_{n^*} for (n^*, ^{3}He*) recoil angle: 0° to 180° (MeV)
Initial: photoneutron heating creating d^*	(n, d^*)	3[b]	0.145 (average photo neutron energy; 2.9 MeV Beam)	0.064 (average d^*, 2.9 MeV Beam)	0.145	N/A
Gen 1: Fusion Reaction with heated d^* as projectile	^{2}H$(d^*, n^*)^3$He ^{3}H $(d^*, p^*)^3$H	0.017[c]	N/A	0.064	3.33	2.2 to 2.76
Fusion neutron heating of d^*	(n, d^*)	2.3[d]	2.2–2.76	0.98–1.27	4.25–4.54	N/A
Gen 2: subsequent fusion reaction with d^* as projectile	^{2}H$(d^*, n)^3$He	0.1[e]	N/A	0.98–1.27	4.25–4.54	1.77–4.12 (for d^* = 0.98 MeV) 1.72–4.45 (for d^* = 1.27 MeV)

[a]Q is energy released by reaction.
[b]Nuclear Energy Agency: JANIS Books. 2015. http://www.oecd-nea.org/janis/book/ (Accessed Aug. 14, 2018).
[c]Calculated screened (dD) cross section as found in Ref. [12].
[d]Nuclear Energy Agency: JANIS Books. 2015. http://www.oecd-nea.org/janis/book/ (Accessed Aug. 14, 2018).
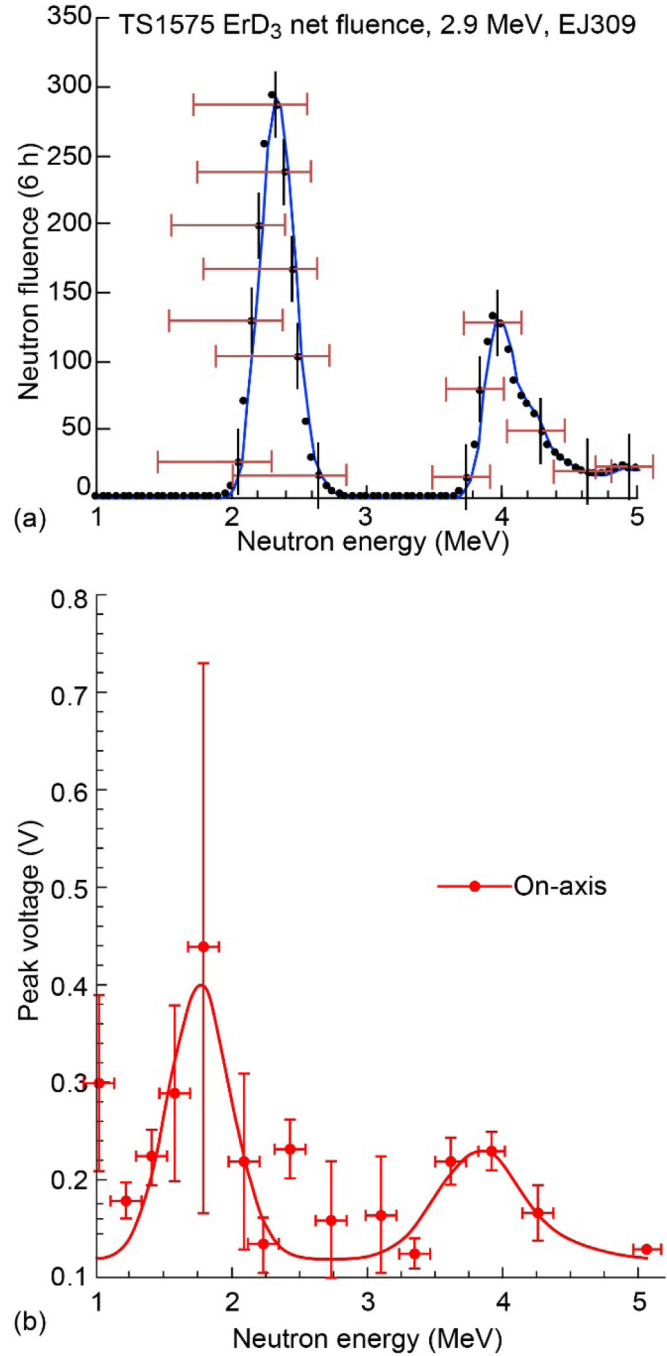[e]EXFOR Nuclear Database (Accessed Aug. 14, 2018).

FIG. 7. Comparison of neutron spectra from (a) current work bremsstrahlung radiation of deuterated samples (TS1575 6 h exposure) and (b) inertial confinement fusion aggregation of nine shots, TOF detectors on-axis [31]. Original content from Ref. [31] IOP work may be used under the terms of the Creative Commons Attribution 3.0 license. Any further distribution of this work must maintain attribution to the author(s) and the title of the work, journal citation and DOI.

potentially resulting from subsequent fusion reactions. Kinematic derivations for neutron heating of the deuteron performed in Ref. [12] were used to calculate the range of neutron energies caused by the heated fuel (Table IV). Bremsstrahlung

TABLE V. Factors influencing detector efficiency for measuring fusion (2.45 MeV) neutron counts. Absolute detector efficiency (last column) equals product of preceeding columns.

Detector	Detector intrinsic efficiency	Filters (PU, FFT and, baseline RMS)[c]	Template matching	8σ	Cave factor (neutrons passing through cave)[d]	Geometric factor[e]	Absolute detector efficiency (product)
			PSD				
EJ309	0.49[a]	0.65	0.88	0.42	0.20	0.0003	7×10^{-6}
stilbene	0.21[b]	0.82	0.94	0.78	0.20	0.00007	2×10^{-6}

[a]110 keVee threshold.

[b]40 keVee threshold.

[c]PU (Pile Up), FFT (Fast Fourier Transform), RMS (root mean square).

[d]MCNP® calculations determined that the lead/B-PE cave scattered 80% of fusion energy neutrons away from the detectors permitting 20% transmission. It is noted that scattered neutrons reaching the detectors will lose less than 0.5% of their energy if scattered off of Pb nuclei.

[e]Assumes isotropic, point neutron source. Detectors located perpendicular to the beam scan direction at distance of $d = 76$ cm, EJ-309 detector radius, $r_1 = 2.5$ cm and, stilbene detector radius $r_2 = 1.25$ cm. Geometric scale factor: $\varepsilon_G = 1/2(1 - d/\sqrt{d^2 + r^2})$.

at 2.9 MeV gives rise to photoneutrons with an average energy of 0.145 MeV. Neutron-deuteron recoil then creates a hot deuteron with average energy of 0.064 MeV. Given enhanced screening as noted by Pines *et al.* [12], a hot deuteron may fuse with a cold deuteron. The separation angle of the $(n, {}^3\text{He})$ recoil products from $0°$–$180°$ leaves the neutron with 2.2–2.76 MeV. This energy spread coupled with the full width at half maximum (FWHM) of the instrument explains some of the broadening of the neutron peaks. The table also provides the resulting neutron energies for various projectile particles, with product energies consistent with either ${}^2\text{H}(d^*, p^*){}^3\text{H}$ or ${}^2\text{H}(d^*, n^*){}^3\text{He}$. A second-generation fusion neutron heats a deuteron (n, d^*), increasing fusion neutron energies from 1.72–4.45 MeV, which may result in the secondary peak and shoulder of 4–4.2 MeV, noted in Figs. 5(a) and 5(b).

2. Efficiency of detecting fusion neutrons

From the point at which the fusion neutrons are created until they are counted in the detector, there are several loss mechanisms. Table V lists the factors influencing detector efficiency for each of the mechanisms considered. These factors include detector intrinsic efficiency, three data postprocessing factors, a cave factor (neutrons passing through cave), and a geometric factor. The data postprocessing factors account for effects of the filter, template matching, and the 8σ cut. The final column tabulates absolute detector efficiency, which is the product of the noted factors for both the EJ-309 and stilbene. Based on these analyses, for every 1×10^6 fusion energy neutrons created the EJ-309 would measure ≈ 7 neutrons, and the stilbene would measure ≈ 2 neutrons.

3. Other enhanced nuclear reactions

Figures 5 and 6 show evidence of distinct peaks of neutrons having ≈ 4 and ≈ 5 MeV energies. The 4-MeV peak appears sharp, potentially indicating unique nuclear reactions and not simple energy boosting from hot fuel reactions (i.e., (n, d^*) followed by (d^*, n)). Examining Fig. 4(a), these higher-energy neutrons correspond to PSD counts in the ≈ 1000–1500 keVee range. To confirm these counts were not caused

by intense (n, γ) reactions with the surrounding materials, the LaBr_3 spectrum was examined in this energy range and revealed a monotonically decreasing spectrum with no structure, thus mitigating concerns of γ leakage into the neutron channel.

In the highly deuterated metal lattice, which provides shell and lattice screening coupled with the temporal plasma filaments from the γ radiation, it appears that other processes (for example Oppenheimer-Phillips [13] stripping processes in the highly screened environment) occurred where a fast neutron is ejected, and the proton fuses with the metal nuclei. Using the methods in Ref. [12], Pines *et al.* calculated very large enhancement factors, on the order of 10^{13} above bare cross sections, given the ${}^{166}\text{Er}$ shell and photon-induced plasma screening. Consequently, 50- to 60-keV deuterons may react with the lattice atoms.

Table VI presents candidate reactions with host metal isotopes. One can see for erbium that several reactions may result in 4-MeV neutrons (e.g., ${}^{166}\text{Er}(d, n){}^{167}\text{Tm}$ or ${}^{166}\text{Er}({}^3\text{He}, n){}^{168}\text{Yb}$) or 5-MeV neutrons (e.g., ${}^{170}\text{Er}(d, n){}^{171}\text{Tm}$ or ${}^{168}\text{Er}({}^3\text{He}, n){}^{170}\text{Yb}$). For titanium, 4-MeV neutrons may result from ${}^{46}\text{Ti}(d, n){}^{47}\text{V}$, and 5-MeV neutrons from ${}^{47}\text{Ti}(d, n){}^{48}\text{V}$. Table VI also indicates if the product is stable and gives the decay half-life, if unstable. The stable isotopes would not be seen during the posttest HPGe γ scans, nor would the isotopes with longer half-lives. Postexposure HPGe γ analyses did not reveal isotopes other than ones obtained via neutron capture.

Based on the above observations, it appears that both primary d-D fusion and Oppenheimer-Phillips stripping processes in the highly screened environment occurred. Evidence of these energetic neutrons indicates attractive nuclear processes are occurring with energetic products (n^*, p^*, t^*, ${}^3\text{He}^*$), which can result in subsequent nuclear processes.

B. Comparison of current deuteron heating to published work

Mori *et al.* [31] conducted direct-drive inertial confinement fusion (ICF) experiments with deuterated polystyrene spheres. Using a three-step pulse, Mori observed that deuteron heating

TABLE VI. Possible reactions with base metal, resulting in fast-neutron emissions.[a]

Reaction	Base metal/natural abundance (%)	Q-value (MeV)	Projectile	Projectile energy (Mev)	Average neutron kinetic energy (Mev)	Notes: (Decay: half life)
^{166}Er$(d, n)^{167}$Tm	^{166}Er/33.61	2.68	d	**1.27**	**3.91**	^{167}Tm: Unstable (electron capture: 9.25 d)
^{167}Er$(d, n)^{168}$Tm	^{167}Er/22.93	3.09	d	1.27	4.32	^{168}Tm: Unstable (positron decay: 93 d)
^{168}Er$(d, n)^{169}$Tm	^{168}Er/26.78	3.35	d	1.27	4.58	^{169}Tm: Stable
^{170}Er$(d, n)^{171}$Tm	^{170}Er/14.93	4.17	d	**0.87**	**5.00**	^{171}Tm: Unstable (β decay: 1.92 yr)
^{170}Er$(d, n)^{171}$Tm	^{170}Er/14.93	4.17	d	**1.27**	**5.39**	^{171}Tm: Unstable (β decay: 1.92 yr)
^{166}Er$(^{3}$He$, n)^{168}$Yb	^{166}Er/33.61	3.50	^{3}He	**0.4**	**4.00**	^{168}Yb: Stable
^{168}Er$(^{3}$He$, n)^{170}$Yb	^{168}Er/26.78	4.63	^{3}He	**0.4**	**5.00**	^{170}Yb: Stable
^{170}Er$(^{3}$He$, n)^{172}$Yb	^{170}Er/14.93	6.01	^{3}He	0.82	6.77	^{172}Yb: Stable
^{46}Ti$(d, n)^{47}$V	^{46}Ti/8.25	2.94	d	**1.2**	**4.03**	^{47}V: Unstable (positron decay: 32.6 min)
^{47}Ti$(d, n)^{48}$V	^{47}Ti/7.44	4.61	d	**0.40**	**4.91**	^{48}V: Unstable (positron decay: 15.9 d)

[a]Bold entries correspond to reactions that may result in the neutron peaks in Figs. 5 and 6.

had occurred. Detailed time-of-flight neutron measurements along the axis ($0°$) and off-axis ($90°$) indicated both fusion energies ($90°$) and neutrons having greater than fusion energy. Figure 7 compares neutron spectra from the current work [Fig. 7(a)] to Mori's on-axis ($0°$) results [Fig. 7(b)] where he claims deuteron heating occurred, resulting in higher-energy neutrons. Although Mori does not highlight it, there is evidence of 2.45-MeV neutrons even on the on-axis case. Similarly, the peak at 1.8 MeV attributed by Mori to ^{12}C$(d, n)^{13}$N may include neutrons that have cooled by deuteron heating. One can see there is some evidence in both plots of neutrons in the 4 MeV range. In Ref. [31], the nominal 4-MeV peak shows a relatively broad base and seems to be consistent with boosted neutrons resulting from deuteron heating with energy ranges consistent with those in Table IV. However, note that the 4-MeV peak in Fig. 7(a) rises very sharply, which suggests that there is a primary reaction, such as screened Oppenheimer-Phillips stripping processes, consistent with the candidate reactions in Table VI.

C. Comparison of measured and theoretical calculations

1. d-D fusion rates, calculation

Using the methods outlined in Pines *et al.* [12], we determined an estimate of the *d*-D fusion rates for the following conditions: 2.9-MeV beam energy and 450-μA current for each of the 16 vials. The calculations were performed in *Mathematica* [32] using the following steps: (i) calculation of the bremsstrahlung spectrum from 0–2.9 MeV, using the five-term β function approximation with a 2.9-MeV endpoint (see Fig. 3 for spectra); (ii) calculation of the photoneutron energy spectra; (iii) determination of the resulting deuteron energy spectra (from these calculations we note the average photoneutron energy of 145 keV and average hot deuteron energy of 64 keV); and (iv) determination of the number of *d*-D reactions per second per vial, utilizing shell and plasma screening. Of the total number of *d*-D reactions per second, half would have created neutrons via ^{2}H$(d, n)^{3}$He, and the other half would have created protons via ^{2}H$(d, p)^{3}$H.

Utilizing both shell and plasma screening (with screening length $\lambda_{sc} = 4.16 \times 10^{-10}$ cm), we calculate a total reaction rate for all 16 samples of 1.2×10^{3} neutrons/s.

2. d-D reaction rates, experimental

Fusion energy neutron counts scaled to the sample location were determined to be $1.5 \pm 0.3 \times 10^{3}$ neutrons/s for TS1575 and $1.6 \pm 0.3 \times 10^{3}$ neutrons/s for TS1576 via the EJ-309 detector, showing process reproducibility. These values were obtained by scaling the neutron counts integrated in the fusion energy range (nominally 2.0–2.6 MeV) to account for detector factors effecting detector sensitivity of measuring neutron counts as outlined in Table V. The measured neutron rate for the fusion channel energies for all 16 vials compared favorably with the calculated value.

V. SUMMARY

In this work, we demonstrate the impact of efficient electron screening on localized fusion rates in a dense fuel environment. Based on the theoretical insight of the companion work of this study [12], we exploit neutrons to effectively heat deuterons in primary and subsequent reactions with the well-screened cold target fuel, where screening is provided by shell, conduction, or plasma electrons, resulting in *d*-D reactions measured by characteristic fusion energy neutrons. This fusion cycle is performed at high fuel density inside a metal lattice, which enables subsequent reactions with the host metal nuclei and other secondary processes.

Specifically, exposure of deuterated materials including ErD$_3$ and TiD$_2$ to bremsstrahlung photon energies ($\leqslant 2.9$ MeV) resulted in both photodissociation-energy neutrons and neutrons with energies consistent with ^{2}H$(d, n)^{3}$He fusion reactions, and also demonstrated process reproducibility. This study and the one in Ref. [12] identified several key ingredients required for fusion reactions. Deuterated metals present a unique environment with high fuel density (10^{22}–10^{23} D atoms/cm^3), which further increases the fusion reaction probability through shell and lattice electron

screening, reducing the *d*-D fusion barrier. Exposing deuterated fuels to a high-photon flux enhanced screening conditions near the cold D fuel. This additional screening further increases the Coulomb barrier transparency and further enhances fusion reaction rates. In these tests, deuterons were initially heated by photoneutrons with an average energy of 145 keV from the 2.9-MeV beam energy to initiate fusion. However, other neutron sources would also provide the necessary deuteron kinetic energy. Calculations in the companion paper [12] indicate that neither electrons nor photons alone impart sufficient deuteron kinetic energy to initiate measurable *d*-D reactions.

Neutron spectroscopy revealed that both *d*-D 2.45-MeV fusion neutrons were produced and other processes occurred. The data indicate that the significant screening enabled charged reaction products hot d^* or ^{3}He* to interact with the host metal. These interactions may produce the $\approx$4- and $\approx$5-MeV neutrons where Oppenheimer-Phillips stripping processes occurred in the strongly screened environment, capturing the proton and ejecting the neutron. The current work demonstrates the ability to create enhanced nuclear reactions in highly deuterated metals with the deuteron fuel in a stationary center-of-mass frame. This process eliminates the need to accelerate the deuteron fuel into the target with implications for several practical applications.

VI. FUTURE WORK

The current tests demonstrate the feasibility of initiating fusion reactions with simple, relatively inexpensive equipment. Ideally, these experiments should be repeated in the future with a pulsed beam to further validate the *d*-D fusion reactions and to further resolve the source of the higher-energy neutrons. The pulsed beam would allow use of time-of-flight instrumentation (not possible with the continuous wave beam

used herein) to further corroborate the neutron energy measurements.

By following the described procedure with a precision γ beam it is possible to control neutron and deuteron energies to examine primary and boosted fusion and screened Oppenheimer-Phillips processes over a wide energy range. Nuclear cross sections can be established as a function of beam/deuteron energy and host materials. Process scale up using an energy-efficient LINAC, may lead to a new means of generating or boosting medical and industrial isotope production.

---

[1] A. Huke, Ph.D. thesis, Technische Universität Berlin, 2002.

[2] A. Huke, K. Czerski, P. Heide, G. Ruprecht, N. Targosz, and W. Zebrowski, Phys. Rev. C **78**, 015803 (2008).

[3] K. Czerski, A. Huke, P. Heide, M. Hoeft, and G. Ruprecht, Nuclei in the Cosmos V, in *Proceedings of the International Symposium on Nuclear Astrophysics*, edited by N. Prantzos and S. Harissopulos (Editions Frontières, Volos, Greece, 1998), p. 152.

[4] K. Czerski, A. Huke, A. Biller, P. Heide, M. Hoeft, and G. Ruprecht, Europhys. Lett. **54**, 449 (2001).

[5] F. Raiola *et al.*, Eur. Phys. J. A **13**, 377 (2002).

[6] F. Raiola *et al.*, Phys. Lett. B **547**, 193 (2002).

[7] V. M. Bystritskii, G. Dudkin, M. Filipowicz, J. Huran, A. Krylov, B. Nechayev, V. Padalko, F. Pen'kov, A. Philippov, and Y. Tuleushev, Phys. Part. Nucl. Lett. **13**, 79 (2016).

[8] H. J. Assenbaum, K. Langanke, and C. Rolfs, Z. Phys. A **327**, 461 (1987).

[9] U. Greife, F. Gorris, M. Junker, C. Rolfs, and D. Zahnow, Z. Phys. A **351**, 107 (1995).

[10] F. Strieder, C. Rolfs, C. Spitaleri, and P. Corvisiero, Naturwissenschaften **88**, 461 (2001).

[11] C. Bonomo, G. Fiorentini, Z. Fulop, L. Gang, G. Gyurky, K. Langanke, F. Raiola, C. Rolfs, E. Somorjai, F Strieder, J. Winter, and M. Aliotta, Nucl. Phys. A **719**, C37 (2003).

[12] V. Pines *et al.*, Phys. Rev. C **101**, 044609 (2020).

[13] J. R. Oppenheimer and M. Phillips, Phys. Rev. **48**, 500 (1935).

[14] B. M. Steinetz *et al.*, NASA/TM—2017-218963, 2017.

[15] T. L. Benyo, B. M. Steinetz, R. C. Hendricks, R. E. Martin, L. P. Forsley, C. C. Daniels, A Chait, V. Pines, M. Pines, and N. Penney, NASA/TM—2015-218491 REV1, 2017.

[16] V. B. Belyaev, M. B. Miller, J. Otto, and S. A. Rakityansky, Phys. Rev. C **93**, 034622 (2016).

[17] A. Y. Didyk and R. Wisniewski, Phys. Particles Nuclei Lett. **10**, 273 (2013).

[18] Yu. A. Kaschuck, B. Esposito, L. A. Trykov, and V. P. Semenov, Nucl. Instrum. Methods A **476**, 511 (2002).

[19] M. Z. Tarasko, A. Soldatov, and V. Rudnikov, At. Energy **65**, 858 (1988).

[20] D. B. Pelowitz, Los Alamos National Laboratory LA-CP-11-00438, 2011.

[21] A. Wattenberg, Argonne National Laboratory Preliminary Report No. 6, 1949.

[22] J. K. Polack, M. Flaska, A. Enqvist, C. Sosa, C. Lawrence, and S. Pozzi, Nucl. Instrum. Methods A **795**, 253 (2015).

[23] M. A. Norsworthy, A. Poitrasson-Rivière, M. Ruch, S. Clarke, and S. Pozzi, Nucl. Instrum. Methods A **842**, 20 (2017).

[24] A. C. Kaplan, M. Flaska, A. Enqvist, J. L. Dolan, and S. A. Pozz, Nucl. Instrum. Methods A **729**, 463 (2013).

[25] S. Yousefi, L. Lucchese, and M. D. Aspinall, Nucl. Instrum. Methods A **598**, 551 (2009).

[26] M. D. Aspinall, B. D'Mellow, R. O. Mackin, M. J. Joyce, N. P. Hawkes, D. J. Thomas, Z. Jarrah, A. J. Peyton, P. J. Nolan, and A. J. Boston, Nucl. Instrum. Methods A **583**, 432 (2007).

[27] I. A. Pawelczak, S. A. Ouedraogo, A. M. Glenn, R. E. Wurtz, and L. F. Nakae, Nucl. Instrum. Methods A **711**, 21 (2013).

[28] M. Matzke, Physikalisch-Technische Bundesanstalt, 2012, https://rsicc.ornl.gov/codes/ccc/ccc7/ccc-799.html.

[29] T. Goorley, Los Alamos National Laboratory, LA-UR-14-24680, 2014.

[30] R. F. Lang, J. Pienaar, E. Hogenbirk, D. Masson, R. Nolte, A. Zimbal, S. Röttger, M. Benabderrahmane, and G. Bruno, Nucl. Instrum. Methods A **879**, 31 (2017).

[31] Y. Mori *et al.*, Nucl. Fusion **57**, 116031 (2017).

[32] Wolfram, *Mathematica*, ver. 11, 2018, http://www.wolfram.com/mathematica/.